Enabling Fast Photoresponse in Hybrid Perovskite/MoS_2 Photodetectors by Separating Local Photocharge Generation and Recombination

*Jingfeng Song,[1†] Tianlin Li,[1†] Wenhao Li,[2] Zhiyong Xiao,[1] Bo Chen,[3] Dawei Li,[1,4] Stephen Ducharme,[1] Yongfeng Lu,[4] Jinsong Huang,[3] Rashid Zia,[2] and Xia Hong[1]**

[1] Department of Physics and Astronomy & Nebraska Center for Materials and Nanoscience, University of Nebraska-Lincoln, Lincoln, NE 68588, USA

[2] School of Engineering, Brown University, Providence, RI 02912, USA

[3] Department of Applied Physical Sciences, University of North Carolina-Chapel Hill, Chapel Hill, NC 27599, USA

[4] Department of Electrical and Computer Engineering, University of Nebraska-Lincoln, Lincoln, NE 68588, USA

[*] E-mail: xia.hong@unl.edu

[†] These authors contributed equally to this work.

KEYWORDS: hybrid perovskites, two dimensional semiconductors, photodetectors, photocharge dynamics, scanning photocurrent microscopy, time-resolved photoluminescence

Abstract:

Interfacing $CH_3NH_3PbI_3$ ($MAPbI_3$) with two-dimensional van der Waals materials in lateral photodetectors can suppress the dark current and driving voltage, while the interlayer charge separation also renders slower charge dynamics. In this work, we show that more than one order of magnitude faster photoresponse time can be achieved in $MAPbI_3/MoS_2$ lateral photodetectors by locally separating the photocharge generation and recombination through a parallel channel of single-layer $MAPbI_3$. Photocurrent (I_{ph}) mapping reveals electron diffusion lengths of about 20 μm in single-layer $MAPbI_3$ and 4 μm in $MAPbI_3/MoS_2$ heterostructure. The power scaling of I_{ph} and time-resolved photoluminescence studies point to the dominant roles of the heterostructure region in photogeneration and single-layer $MAPbI_3$ in charge recombination. Our results shed new lights on the material design that can concurrently enhance photoresponsivity, reduce driving voltage, and sustain high operation speed, paving the path for developing high performance lateral photodetectors based on hybrid perovskites.

The organolead trihalide perovskites such as $CH_3NH_3PbI_3$ ($MAPbI_3$) have received significant research interest over the past decade due to their high power conversion efficiency,[1-3] strong solar absorption,[1, 2] board-spectrum photoresponse,[4, 5] and long charge diffusion lengths,[6, 7] making them promising for developing high-performance photovoltaic and optoelectronic devices. Previous studies of hybrid perovskite-based photodetectors have focused on the vertical device configuration, which requires high sample uniformity and full coverage of the active layers with large area electrodes.[8] The presence of the top electrode also reduces the efficiency of light adsorption. There have been emerging interests in developing lateral-structure photodetectors for their simplified production, high responsivity, and compatibility with flexible substrates.[8] For hybrid perovskite photodetectors, however, adopting the lateral structure yields higher dark current and requires larger driving voltage due to the lack of a charge blocking layer and the large spacing between electrodes.[8-11] To overcome these performance limitations, $MAPbI_3$ has been interfaced with a charge transfer layer, such as two dimensional (2D) van der Waals graphene[12-14] and transition metal dichalcogenide (TMDC),[15-18] to promote charge separation. Even though suppressed dark current (< 1 nA),[16] low drive voltage (down to 1 V),[14] and broad-spectrum response[15-18] have been achieved in these $MAPbI_3$/2D heterostructures, the photoresponse speed is highly compromised (2.7 ms-20s)[9-11, 15-18] compared with single-layer $MAPbI_3$[8, 19] due to the much slower charge dynamics in the charge depletion region. For technological implementation of perovskite lateral photodetectors, a critical challenge is to satisfy the competing material requirements for enhanced photoresponsivity, small dark current, low driving voltage, and high operation speed.

A possible route to tackle this challenge is to provide parallel conduction channels that spatially separate the dominant photocharge generation and recombination processes. For example, when a

hybrid perovskite/2D heterostructure is under detailed balance with a single-layer hybrid perovskite, it is possible to harness the enhanced photoresponsivity in the former channel, with the charge dynamics dominated by the fast recombination in the latter. By gaining microscopic understanding of the various charge processes and assessing the critical length and time scales, one can anchor the parameter space for optimized device performance.[20, 21]

In this work, we report fast photoresponse in high performance lateral photodetectors consisting of parallel $MAPbI_3$/few-layer MoS_2 heterostructure and single-layer $MAPbI_3$ channels (Figure 1a). The devices exhibit high photoresponsivity (~1,200 A W^{-1}) with low dark current (< 5 pA) under ultralow driving voltage (0.2 V). Photocurrent (I_{ph}) mapping via scanning photocurrent microscopy (SPCM) shows that I_{ph} in the heterostructure region is about 40 times higher than that in single-layer $MAPbI_3$. The electron diffusion lengths are about 20 μm in single-layer $MAPbI_3$ and 4 μm in $MAPbI_3$/MoS_2 heterostructure. The photocurrent switching under global illumination reveals rising and decay time of about 200 μs, more than one order of magnitude faster than those reported in lateral photodetectors based on hybrid perovskite/2D heterostructures. The illumination power scaling of I_{ph} indicates a fast bimolecular radiative recombination in single-layer $MAPbI_3$ and a slow quadruple molecular process in $MAPbI_3$/MoS_2. Time-resolved photoluminescence (TRPL) studies yield a faster timescale for charge separation in the heterostructure (31±13 ns) than charge recombination in $MAPbI_3$ (96±19 ns), confirming that the device response is dominated by the latter under detailed balance. Our study provides important material parameters for designing hybrid perovskite-based lateral photodetectors that can concurrently enhance photoresponsivity, reduce dark current and driving voltage, and sustain high operation speed.

Results and Discussion. We interfaced few-layer MoS_2 with $MAPbI_3$ for constructing the hybrid photodetectors. Compared with monolayer MoS_2, few-layer MoS_2 possesses smaller Schottky barrier height (< 0.05 eV) with the metal contact (Ti/Au),[22] which enhances the collection efficiency of photogenerated carriers at electrodes. Their higher density of states also promote enhanced interlayer charge transfer of photocarriers from $MAPbI_3$.[16] On the other hand, it is desirable to have the MoS_2 layer fully depleted to achieve suppressed dark current and enhanced photoresponsivity. The upper bound of MoS_2 thickness is thus imposed by the Thomas-Fermi screening length.

We mechanically exfoliated 3-5 nm MoS_2 flakes (5-7 layer) onto SiO_2/Si substrates, with the layer thickness identified by Raman spectroscopy[23] (Figure S1, Supporting Information) and atomic force microscopy (AFM). Selected MoS_2 flakes were fabricated into two-point devices using e-beam lithography followed by metal deposition (10 nm Ti/50 nm Au). The electrode length is about twice of the width of MoS_2 flake to enable parallel conduction channels. After depositing 500 nm thick $MAPbI_3$ on the device via spin coating, the sample was annealed at 100 °C.[24, 25] X-ray diffraction (XRD) θ-2θ scan (Figure 1b) shows that the $MAPbI_3$ film is polycrystalline with dominating (110)-orientation of the tetragonal phase (a = 8.90 Å, c = 12.61 Å). Figure 1c shows the optical image of a $MAPbI_3$ coated 5-layer MoS_2 device. AFM topography images reveal smooth surface morphology of $MAPbI_3$ in regions on MoS_2, SiO_2, and Au (Figure 1d), with a root-mean-square roughness of about 19 nm. The data reported was obtained from three devices, denoted as D1, D2, and D3.

Figure 1e shows the dark current (I_{dark}) vs driving voltage V_{SD} taken on device D1 between the drain (D) and source (S) electrodes before and after the $MAPbI_3$ deposition. With $MAPbI_3$, I_{dark} becomes more than six times smaller, which can be attributed to the band alignment between

$MAPbI_3$ and MoS_2 induced charge depletion (Figure 1f). Few-layer MoS_2 has a band gap of about ~1.4 eV[26] and is electron-doped,[27] while $MAPbI_3$ is slightly hole-doped with a band gap of ~1.6 eV (Figure S2, Supporting Information).[28, 29] Assuming the Fermi energy (E_F) is 0.1 eV below the conduction band minimum (E_C) for MoS_2[30] and 0.7 eV above the valence band maximum (E_V) for $MAPbI_3$,[28, 29] we deduced a depletion width of about 10 μm for $MAPbI_3$ and a Thomas-Fermi screening length of about 7.7 nm for few-layer MoS_2 (Section 3, Supporting Information). These values are much larger than the layer thickness, confirming that the entire sample is in the depletion region. The large built-in electric field (~10^3 V/cm) can thus facilitate efficient charge separation for photogenerated electron-hole pairs.[31]

Next, we map out the source-drain current (I) on device D1 via SPCM, a technique widely used to characterize charge drift, diffusion, and local accumulation in semiconductor nanowires and thin films.[20] Figure 2a shows the spatially resolved photocurrent ($I_{ph} = I - I_{dark}$) at $V_{SD} = 0.2$ V ($I_{dark} = 4.5$ pA). Compared with the single-layer $MAPbI_3$, the $MAPbI_3/MoS_2$ heterostructure region shows significantly higher I_{ph}. Along an equipotential line of the device, I_{ph} decreases by a factor of 10 across the MoS_2 edge over a length of about 20 μm (Figure 2b). The enhanced photocurrent in the heterostructure can be attributed to the suppressed photocarrier recombination. In our device structure, the light absorption and photocarrier generation occur mostly in the 500 nm $MAPbI_3$ top layer,[17] and the built-in electric field facilitates efficient transfer of photogenerated electrons into MoS_2. The interlayer charge separation can effectively prevent electron-hole recombination, which significantly extends the carrier lifetime, leading to higher photocarrier density and thus enhanced photocurrent.[15, 16, 31, 32] The charge transfer effect is supported by the reduced photoluminescence (PL) intensity for the 1.6 eV $MAPbI_3$ exciton in the heterostructure[16] (Figure S2, Supporting Information).

Beyond a few micron distance from the MoS_2 edge, I_{ph} exhibits an exponential decay:

$$I_{\mathrm{ph}} \propto \exp(-x/L_D), \quad (1)$$

where x is the position of laser excitation and L_D is the decay length. In single-layer $MAPbI_3$, this variation reflects the diffusion of photocarriers into the heterostructure region, where radiative recombination is suppressed. As $MAPbI_3$ is *p*-type, the diffusion current is dominated by the minority electrons. Fitting the photocurrent to Equation 1, we deduced a diffusion length for electrons in $MAPbI_3$ of $L_{MAPI,e}$ = 20.2 μm. This value is close to previously reported minority diffusion length in $MAPbI_3$ polycrystalline films,[33-35] single crystalline nanowires,[36] and bulk single crystals[37] under similar illumination, confirming the high quality of our $MAPbI_3$ samples. A similar mechanism may contribute to the exponential growth of I_{ph} inside the heterostructure region, where the diffusion of photocarriers into the single-layer $MAPbI_3$ region would effectively reduce the net photocurrent. As the photogenerated electrons will be swept into MoS_2, the diffusion current in the heterostructure will be dominated by holes in $MAPbI_3$, and we deduced a corresponding diffusion length of $L_{hetero,h}$ = 16.3 μm.

We also examined the I_{ph} profile along the current direction (Figure 2c). Between the source and drain electrodes, I_{ph} is ununiform and asymmetric in both the single-layer $MAPbI_3$ and heterostructure regions: the maximum I_{ph} occurs within the channel, and the drain electrode side exhibits a higher I_{ph} level compared with the source electrode side. Similar channel I_{ph} variation has been observed in previous SPCM studies of hybrid perovskite,[36] reflecting the net contribution of drift and diffusion current of photogenerated electron and holes.[20, 38, 39] In the single-layer region, as the diffusion length of $MAPbI_3$ well exceeds the channel length, the current variation is determined by the drift current. Such an asymmetric profile suggests a higher hole mobility, as expected for *p*-doped $MAPbI_3$.[35, 37] In the heterostructure region, due to the interlayer charge

separation, the I_{ph} distribution reflects the higher hole mobility in $MAPbI_3$ compared to the electron mobility in MoS_2, consistent with our sample characterizations.[24, 40, 41]

The photocurrent decay beyond the two electrode regions is also highly asymmetric. In the heterostructure region, I_{ph} is significantly suppressed and shows a dip in the vicinity of the source electrode due to the effective cancelation of hole drift current in $MAPbI_3$ with the electron diffusion current in MoS_2. In single-layer $MAPbI_3$, such cancellation does not occur due to the Schottky contact with Au for electrons.[20] Beyond the drain electrode, I_{ph} is dominated by electron diffusion and decays exponentially in both regions, with a decay length of 21.0 μm (3.96 μm) in the single-layer $MAPbI_3$ (heterostructure).[20, 36] The electron diffusion length for $MAPbI_3$ agrees well with $L_{MAPI,e}$ extracted from the channel region (Figure 2b). The value in the heterostructure is consistent with the electron diffusion length in MoS_2 obtained via SPCM[42] and PL imaging.[43]

Figure 3a shows I_{ph} vs laser power (P) taken on device D1 under local and global illumination (Figure S3, Supporting Information). For both conditions, I_{ph} exhibits a power-law dependence on P, $I_{\mathrm{ph}} = \alpha P^{\beta}$, suggesting that the sample has reached the detailed balance between the photocharge generation rate ($\propto P$) and recombination rate (U_{rec}).[44] Here the prefactor α is a fitting parameter, and the exponent β characterizes the dominating charge recombination process.[45] Under local illumination, I_{ph} in the single-layer $MAPbI_3$ exhibits $\beta_{MAPI} = 0.51\pm0.02$, agreeing well with the theoretical value of ½ for the bimolecular band-to-band recombination (Figure 3b). In this scenario, U_{rec} is proportional to the density product for the electron (n) and hole (p), leading to a quadratic dependence on the photocarrier density (Section 5, Supporting Information). In contrast, I_{ph} in the heterostructure region possesses $\beta_{hetero} = 0.24\pm0.01$, pointing to a distinct charge annihilation mechanism. Due to the interlayer charge separation, the monomolecular processes

(*e.g.*, exciton annihilation) and bimolecular processes (electron-hole recombination) in both layers are significantly suppressed, and the higher-order charge recombination processes such as excitonic complexes involving quadruple charges[46, 47] become dominant. As illustrated in Figure 3c, photogenerated electrons in $MAPbI_3$ drifted to the interface can pair with holes, forming instant excitonic complexes with out-of-plane electric dipole moments. Their annihilation can be facilitated by the dipole-dipole interaction, resulting in an effective quadruple molecular process. The corresponding U_{rec} scales as n^2p^2, leading to an exponent $\beta = ¼$. Such recombination processes are localized around the interface and have been observed previously in charge-separated graphene,[14, 31] few-layer MoS_2,[32] and semiconductor nanowires on substrates.[20] The small error bars for the fitting parameters α and β over a broad power range confirm the robustness of the bimolecular and quadrupole charge recombination processes (Section 4, Supporting Information).

What is interesting is the power scaling of photocurrent under global illumination, with the excited area consisting of both single-layer $MAPbI_3$ and heterostructure regions. Within the measured power range, the global I_{ph} is over one order of magnitude higher than the local I_{ph} in single-layer $MAPbI_3$. Considering the small device area (~570 μm^2) compared with the laser spot (800 μm diameter), only a small fraction of the photons (~0.1%) in global illumination can participate in photocarrier generation within the channel. The high global I_{ph} confirms the dominating contribution from the heterostructure region (Figure 3a). On the other hand, the power scaling exponent for global I_{ph} is 0.474±0.006, close to 0.5 and similar to that for single-layer $MAPbI_3$, indicating that the detailed balance of the entire device area is dominated by bimolecular charge recombination in the single-layer $MAPbI_3$ region. This spatial separation between photocarrier generation and annihilation processes can be explained by the higher probability of the two-particle process in single-layer $MAPbI_3$ than four-particle process in $MAPbI_3/MoS_2$, as

depicted by the Fermi's golden rule (Section 5, Supporting Information). We then calculated the photoresponsivity $R = I_{ph}/P_{eff}$ under global illumination, with P_{eff} the effective illumination power on the conducting channel. At a driving voltage of V_{SD} = 0.2 V, R is maximized at the lowest measured power, reaching 1.2×10^3 A W^{-1}, comparable with previously reported values in $MAPbI_3$/TMDC heterostructures.[15-18] Using the shot noise approximation $R = D^* \times (2eI_{\mathrm{dark}})^{1/2}$,[8] we deduced the corresponding detectivity D^* of about 10^{18} Jones. This value is significantly higher than the reported values due to the much lower dark current ($I_{\mathrm{dark}} = 4.5$ pA) in our device.

The existence of bimolecular recombination process in our device due to the parallel single-layer channel can facilitate a high-speed photocurrent response. Figure 4a shows the I_{ph} switching in device D1 under global illumination of a pulsed laser, which exhibits consistent on/off behaviors. By fitting multiple I_{ph} switching periods to the exponential time dependence (Figure 4b):

$$I_{\mathrm{ph}} \propto \begin{cases} 1 - \exp\left(-\frac{\Delta t}{\tau_r}\right) & \text{(light on)} \\ \exp\left(-\frac{\Delta t}{\tau_d}\right) & \text{(light off)} \end{cases}, \qquad (2)$$

we extracted the average photocurrent rising time of τ_r = 209±8 μs and decay time of τ_d = 229±8 μs. The response time is more than one order of magnitude faster than that of the $MAPbI_3$/TMDC heterostructures (> 2.7 ms)[9-13, 15-18] and more than two orders of magnitude faster than that of the $MAPbI_3$/graphene heterostructures (> 28.8 ms).[12-14]

To elucidate the microscopic origin of the high-speed photocurrent response, we performed time-resolved photocurrent measurements in different regions of the device. Figure 4c shows the transient photocurrent in device D2 under local illumination. The measurements taken on two

different spots in the single-layer $MAPbI_3$ region yield highly consistent results, with an average decay time of $\tau_{d,\mathrm{MAPI}} = 164 \pm 15\ \mu s$, comparable with previous results reported in $MAPbI_3$ lateral devices.[8-11] In the heterostructure region, we obtained a slower decay time $\tau_{d,\mathrm{hetero}} = 306 \pm 14\ \mu s$, which can be attributed to charge diffusion to the single-layer region. The fact that the device under global illumination possesses response times τ_r and τ_d between the local values of $\tau_{d,\mathrm{MAPI}}$ and $\tau_{d,\mathrm{hetero}}$ point to the net contributions of both regions in determining the photocurrent. In other words, under detailed balance, while the photocurrent level is dominated by the heterostructure region, the response speed is determined by the convoluted effect of the bimolecular charge annihilation in single-layer $MAPbI_3$ and the charge diffusion between the parallel channels. This scenario naturally explains the I_{ph} vs P scaling under global illumination (Figure 3a), where the I_{ph} enhancement and recombination dynamics are associated with distinct origins.

To evaluate the individual time scales of charge recombination in the single-layer $MAPbI_3$ and interlayer charge separation in the heterostructure, we conducted local time-resolved photoluminescence measurements. Figure 5a shows the normalized PL intensity vs time taken on device D3, with the laser focused on multiple spots along a line cut across the MoS_2 channel (Figure 5a inset). The heterostructure region exhibits significantly faster decay of the PL signal compared with the single-layer $MAPbI_3$ after stimulation. At 100 ns, the former decays to about 5% of initial intensity while the latter possesses about 45% of the initial level. The signals for both the single-layer and heterostructure regions fully recover to their original intensity levels within 400 ns (Figure S5, Supporting Information). Due to the relatively high baseline of the PL signal, it is possible that the PL signal decays to the baseline before the device full recovers.[48, 49] Since the PL signal originates from the photon emission during electron-hole recombination, the fast

decay in the heterostructure reflects the suppressed band-to-band radiative recombination, yielding strong evidence for the interlayer charge separation.[48] We then fitted the local PL decay to a single exponential model.[48] The deduced decay time τ_{PL} characterizes the timescales of charge recombination in the single-layer $MAPbI_3$ and interlayer charge transfer in the heterostructure regions. As shown in Figure 5b, the average τ_{PL} in the single-layer $MAPbI_3$ region is 96±19 ns, consistent with previous TRPL studies of hybrid halide perovskites.[48, 50, 51] The heterostructure region exhibits a reduced τ_{PL} of 31±13 ns. The significantly faster interlayer charge transfer process confirms the lack of radiative recombination process in the power scaling of photocurrent (Figure 3a). The charge recombination time τ_{PL} is significantly smaller than the photoresponse time of the device, showing the device speed is limited by charge diffusion from the heterostructure to the single-layer region. The relative length scales between the dimensions of the parallel channels and charge diffusion lengths thus play a critical role in determining the photocurrent responsibility and response time.

Conclusions. In summary, we have demonstrated a prototype lateral photodetector with high responsivity and fast photoresponse by adopting parallel single-layer $MAPbI_3$ with $MAPbI_3/MoS_2$ heterostructure channels. The I_{ph} switching is more than one order of magnitude faster than those in hybrid perovskite/van der Waals heterostructures. Local photocurrent mapping, power scaling of, and time-resolved photoluminescence measurements collectively point to the distinct origins of enhanced photon current and fast photoresponse, with the former determined by enhanced photocarrier lifetime in the heterostructure region and latter facilitated by the fast radiative recombination in the single-layer $MAPbI_3$. We have also extracted the electron diffusion lengths in both regions, providing important design parameters for optimized device performance. Our

study points to a new material strategy for achieving high photoresponsivity, low driving voltage, and high operation speed in hybrid perovskite-based photodetectors.

Experimental Method. *Scanning photocurrent microscopy*. The scanning photocurrent microscopy studies were carried out in a micro-Raman system with a collimated laser. The photocurrent mapping was generated by measuring the channel current under illumination while scanning the laser spot on the surface of the device. For Figure 2a, we set the laser power of 2 μW with a laser step size of 0.8 μm scanning over an area of 31 μm by 60 μm.

Time-resolved photoluminescence. The sample was excited with a 408 nm, 2.5 MHz repetition rate pulsed laser (PicoQuant, MDL 300) focused by an objective lens (Nikon, CFI Plan Apo Lambda 60XC). The PL signal was collected by the same objective lens and then coupled into a single-mode fiber (Thorlabs, P1-780A-FC-2). Then the PL signal was detected by a single-photon avalanche photodiode (PicoQuant, SPAD) and recorded with a time-correlated single-photon counting system (PicoQuant, PicoHarp 300). For the line scan of the PL lifetime, sample was moved along the *y* axis with a 2.5 μm step size using a piezo stage (MCL, Nano-LPS100).

Supporting Information

Raman Spectrum of Few-Layer MoS_2; Photoluminescence Spectra of Single-Layer $MAPbI_3$ and $MAPbI_3/MoS_2$ Heterostructure; Calculation of Depletion Width and Built-in Electric Field; Illumination Power Dependence of Photocurrent; Modeling of Recombination Dynamics; Time-Resolved Photoluminescence

Acknowledgements

The authors thank Yinsheng Guo and Bo Li for insightful discussions and Shuo Sun and Fei Yang for technical discussions. This work was primarily supported by the National Science

Foundation (NSF) grant numbers DMR-2118828, OIA-2044049, and OIA-1538893, and the Nebraska Center for Energy Sciences Research. JH acknowledges the support of NSF grant number DMR-1903981. The research was performed, in part, in the Nebraska Nanoscale Facility: National Nanotechnology Coordinated Infrastructure, the Nebraska Center for Materials and Nanoscience, and the Nanoengineering Research Core Facility, which are supported by NSF ECCS: 2025298, and the Nebraska Research Initiative.

Conflict of Interest

The authors declare no conflict of interest.

Data Availability

The data that support the findings of this study are available from the corresponding author upon reasonable request.

References

1. Kojima, A.; Teshima, K.; Shirai, Y.; Miyasaka, T. Organometal Halide Perovskites as Visible-Light Sensitizers for Photovoltaic Cells. *Journal of the American Chemical Society* **2009,** *131*, 6050.

2. Green, M. A.; Ho-Baillie, A.; Snaith, H. J. The emergence of perovskite solar cells. *Nature Photonics* **2014,** *8*, 506.

3. Berry, J.; Buonassisi, T.; Egger, D. A.; Hodes, G.; Kronik, L.; Loo, Y.-L.; Lubomirsky, I.; Marder, S. R.; Mastai, Y.; Miller, J. S.; Mitzi, D. B.; Paz, Y.; Rappe, A. M.; Riess, I.; Rybtchinski, B.; Stafsudd, O.; Stevanovic, V.; Toney, M. F.; Zitoun, D.; Kahn, A.; Ginley, D.; Cahen, D. Hybrid Organic–Inorganic Perovskites (HOIPs): Opportunities and Challenges. *Advanced Materials* **2015,** *27*, 5102.

4. Zhang, Y.; Liu, Y.; Yang, Z.; Liu, S. High-quality perovskite $MAPbI_3$ single crystals for broad-spectrum and rapid response integrate photodetector. *Journal of Energy Chemistry* **2018,** *27*, 722.

5. Liu, Y.; Zhang, Y.; Yang, Z.; Ye, H.; Feng, J.; Xu, Z.; Zhang, X.; Munir, R.; Liu, J.; Zuo, P.; Li, Q.; Hu, M.; Meng, L.; Wang, K.; Smilgies, D.-M.; Zhao, G.; Xu, H.; Yang, Z.; Amassian, A.; Li, J.; Zhao, K.; Liu, S. Multi-inch single-crystalline perovskite membrane for high-detectivity flexible photosensors. *Nature Communications* **2018,** *9*, 5302.

6. Shi, D.; Adinolfi, V.; Comin, R.; Yuan, M.; Alarousu, E.; Buin, A.; Chen, Y.; Hoogland, S.; Rothenberger, A.; Katsiev, K.; Losovyj, Y.; Zhang, X.; Dowben, P. A.; Mohammed, O. F.; Sargent, E. H.; Bakr, O. M. Low trap-state density and long carrier diffusion in organolead trihalide perovskite single crystals. *Science* **2015,** *347*, 519.

7. Dong, Q.; Fang, Y.; Shao, Y.; Mulligan, P.; Qiu, J.; Cao, L.; Huang, J. Electron-hole diffusion lengths >175 μm in solution-grown $CH_3NH_3PbI_3$ single crystals. *Science* **2015,** *347*, 967.

8. Wang, H.; Kim, D. H. Perovskite-based photodetectors: materials and devices. *Chemical Society Reviews* **2017,** *46*, 5204.

9. Tian, W.; Zhou, H.; Li, L. Hybrid Organic–Inorganic Perovskite Photodetectors. *Small* **2017,** *13*, 1702107.

10. Zhao, Y.; Zhu, K. Organic–inorganic hybrid lead halide perovskites for optoelectronic and electronic applications. *Chemical Society Reviews* **2016,** *45*, 655.

11. Ahmadi, M.; Wu, T.; Hu, B. A Review on Organic–Inorganic Halide Perovskite Photodetectors: Device Engineering and Fundamental Physics. *Advanced Materials* **2017,** *29*, 1605242.

12. He, M.; Chen, Y.; Liu, H.; Wang, J.; Fang, X.; Liang, Z. Chemical decoration of $CH_3NH_3PbI_3$ perovskites with graphene oxides for photodetector applications. *Chemical Communications* **2015,** *51*, 9659.

13. Lee, Y.; Kwon, J.; Hwang, E.; Ra, C.-H.; Yoo, W. J.; Ahn, J.-H.; Park, J. H.; Cho, J. H. High-Performance Perovskite–Graphene Hybrid Photodetector. *Advanced Materials* **2015,** *27*, 41.

14. Shao, Y.; Liu, Y.; Chen, X.; Chen, C.; Sarpkaya, I.; Chen, Z.; Fang, Y.; Kong, J.; Watanabe, K.; Taniguchi, T.; Taylor, A.; Huang, J.; Xia, F. Stable Graphene-Two-Dimensional Multiphase Perovskite Heterostructure Phototransistors with High Gain. *Nano Letters* **2017,** *17*, 7330.

15. Ma, C.; Shi, Y.; Hu, W.; Chiu, M.-H.; Liu, Z.; Bera, A.; Li, F.; Wang, H.; Li, L.-J.; Wu, T. Heterostructured $WS_2/CH_3NH_3PbI_3$ Photoconductors with Suppressed Dark Current and Enhanced Photodetectivity. *Advanced Materials* **2016,** *28*, 3683.

16. Wang, Y.; Fullon, R.; Acerce, M.; Petoukhoff, C. E.; Yang, J.; Chen, C.; Du, S.; Lai, S. K.; Lau, S. P.; Voiry, D.; O'Carroll, D.; Gupta, G.; Mohite, A. D.; Zhang, S.; Zhou, H.; Chhowalla, M. Solution-Processed MoS_2/Organolead Trihalide Perovskite Photodetectors. *Advanced Materials* **2017,** *29*, 1603995.

17. Kang, D.-H.; Pae, S. R.; Shim, J.; Yoo, G.; Jeon, J.; Leem, J. W.; Yu, J. S.; Lee, S.; Shin, B.; Park, J.-H. An Ultrahigh-Performance Photodetector based on a Perovskite–Transition-Metal-Dichalcogenide Hybrid Structure. *Advanced Materials* **2016,** *28*, 7799.

18. Peng, Z.-Y.; Xu, J.-L.; Zhang, J.-Y.; Gao, X.; Wang, S.-D. Solution-Processed High-Performance Hybrid Photodetectors Enhanced by Perovskite/MoS_2 Bulk Heterojunction. *Advanced Materials Interfaces* **2018,** *5*, 1800505.

19. Chen, B.; Song, J.; Dai, X.; Liu, Y.; Rudd, P. N.; Hong, X.; Huang, J. Synergistic Effect of Elevated Device Temperature and Excess Charge Carriers on the Rapid Light-Induced Degradation of Perovskite Solar Cells. *Advanced Materials* **2019,** *31*, 1902413.

20. Graham, R.; Yu, D. Scanning Photocurrent Microscopy in Semiconductor Nanostructures. *Modern Physics Letters B* **2013,** *27*, 1330018.

21. Maiti, A.; Pal, A. J. Carrier recombination in $CH_3NH_3PbI_3$: why is it a slow process? *Reports on Progress in Physics* **2022,** *85*, 024501.

22. Das, S.; Chen, H.-Y.; Penumatcha, A. V.; Appenzeller, J. High Performance Multilayer MoS_2 Transistors with Scandium Contacts. *Nano Letters* **2013,** *13*, 100.

23. Lee, C.; Yan, H.; Brus, L. E.; Heinz, T. F.; Hone, J.; Ryu, S. Anomalous Lattice Vibrations of Single- and Few-Layer MoS2. *ACS Nano* **2010,** *4*, 2695.

24. Xiao, Z.; Dong, Q.; Bi, C.; Shao, Y.; Yuan, Y.; Huang, J. Solvent annealing of perovskite-induced crystal growth for photovoltaic-device efficiency enhancement. *Advanced Materials* **2014,** *26*, 6503.

25. Song, J.; Xiao, Z.; Chen, B.; Prockish, S.; Chen, X.; Rajapitamahuni, A.; Zhang, L.; Huang, J.; Hong, X. Enhanced Piezoelectric Response in Hybrid Lead Halide Perovskite Thin Films via Interfacing with Ferroelectric $PbZr_{0.2}Ti_{0.8}O_3$. *ACS Applied Materials & Interfaces* **2018,** *10*, 19218.

26. Mak, K. F.; Lee, C.; Hone, J.; Shan, J.; Heinz, T. F. Atomically Thin MoS_2: A New Direct-Gap Semiconductor. *Physical Review Letters* **2010,** *105*, 136805.

27. Li, H.; Yin, Z.; He, Q.; Li, H.; Huang, X.; Lu, G.; Fam, D. W. H.; Tok, A. I. Y.; Zhang, Q.; Zhang, H. Fabrication of Single- and Multilayer MoS_2 Film-Based Field-Effect Transistors for Sensing NO at Room Temperature. *Small* **2012,** *8*, 63.

28. Caputo, M.; Cefarin, N.; Radivo, A.; Demitri, N.; Gigli, L.; Plaisier, J. R.; Panighel, M.; Di Santo, G.; Moretti, S.; Giglia, A.; Polentarutti, M.; De Angelis, F.; Mosconi, E.; Umari, P.; Tormen, M.; Goldoni, A. Electronic structure of $MAPbI_3$ and $MAPbCl_3$: importance of band alignment. *Scientific Reports* **2019,** *9*, 15159.

29. Ou, Q.; Bao, X.; Zhang, Y.; Shao, H.; Xing, G.; Li, X.; Shao, L.; Bao, Q. Band structure engineering in metal halide perovskite nanostructures for optoelectronic applications. *Nano Materials Science* **2019,** *1*, 268.

30. Zhu, W.; Low, T.; Lee, Y.-H.; Wang, H.; Farmer, D. B.; Kong, J.; Xia, F.; Avouris, P. Electronic transport and device prospects of monolayer molybdenum disulphide grown by chemical vapour deposition. *Nature Communications* **2014,** *5*, 3087.

31. Tan, W.-C.; Shih, W.-H.; Chen, Y. F. A Highly Sensitive Graphene-Organic Hybrid Photodetector with a Piezoelectric Substrate. *Advanced Functional Materials* **2014,** *24*, 6818.

32. Wang, X.; Wang, P.; Wang, J.; Hu, W.; Zhou, X.; Guo, N.; Huang, H.; Sun, S.; Shen, H.; Lin, T.; Tang, M.; Liao, L.; Jiang, A.; Sun, J.; Meng, X.; Chen, X.; Lu, W.; Chu, J. Ultrasensitive and Broadband MoS_2 Photodetector Driven by Ferroelectrics. *Advanced Materials* **2015,** *27*, 6575.

33. Wang, X.; Ling, Y.; Chiu, Y.-C.; Du, Y.; Barreda, J. L.; Perez-Orive, F.; Ma, B.; Xiong, P.; Gao, H. Dynamic Electronic Junctions in Organic–Inorganic Hybrid Perovskites. *Nano Letters* **2017,** *17*, 4831.

34. Kim, A.; Son, B. H.; Kim, H. S.; Ahn, Y. H. Direct Measurement of Diffusion Length in Mixed Lead-halide Perovskite Films Using Scanning Photocurrent Microscopy. *Curr. Opt. Photon.* **2018,** *2*, 514.

35. Liu, S.; Wang, L.; Lin, W.-C.; Sucharitakul, S.; Burda, C.; Gao, X. P. A. Imaging the Long Transport Lengths of Photo-generated Carriers in Oriented Perovskite Films. *Nano Letters* **2016,** *16*, 7925.

36. Xiao, R.; Hou, Y.; Fu, Y.; Peng, X.; Wang, Q.; Gonzalez, E.; Jin, S.; Yu, D. Photocurrent Mapping in Single-Crystal Methylammonium Lead Iodide Perovskite Nanostructures. *Nano Letters* **2016,** *16*, 7710.

37. Semonin, O. E.; Elbaz, G. A.; Straus, D. B.; Hull, T. D.; Paley, D. W.; van der Zande, A. M.; Hone, J. C.; Kymissis, I.; Kagan, C. R.; Roy, X.; Owen, J. S. Limits of Carrier Diffusion in n-Type and p-Type $CH_3NH_3PbI_3$ Perovskite Single Crystals. *The Journal of Physical Chemistry Letters* **2016,** *7*, 3510.

38. Fu, D.; Zou, J.; Wang, K.; Zhang, R.; Yu, D.; Wu, J. Electrothermal Dynamics of Semiconductor Nanowires under Local Carrier Modulation. *Nano Letters* **2011,** *11*, 3809.

39. Gu, Y.; Romankiewicz, J. P.; David, J. K.; Lensch, J. L.; Lauhon, L. J. Quantitative Measurement of the Electron and Hole Mobility−Lifetime Products in Semiconductor Nanowires. *Nano Letters* **2006,** *6*, 948.

40. Xiao, Z.; Song, J.; Ferry, D. K.; Ducharme, S.; Hong, X. Ferroelectric-Domain-Patterning-Controlled Schottky Junction State in Monolayer MoS_2. *Physical Review Letters* **2017,** *118*, 236801.

41. Wu, Q.; Wang, K.; Simpson, A.; Hao, Y.; Wang, J.; Li, D.; Hong, X. Electrode Effect on Ferroelectricity in Free-Standing Membranes of $PbZr_{0.2}Ti_{0.8}O_3$. *ACS Nanoscience Au* **2023,** *3*, 482.

42. Wu, C.-C.; Jariwala, D.; Sangwan, V. K.; Marks, T. J.; Hersam, M. C.; Lauhon, L. J. Elucidating the Photoresponse of Ultrathin MoS_2 Field-Effect Transistors by Scanning Photocurrent Microscopy. *The Journal of Physical Chemistry Letters* **2013,** *4*, 2508.

43. Uddin, S. Z.; Kim, H.; Lorenzon, M.; Yeh, M.; Lien, D.-H.; Barnard, E. S.; Htoon, H.; Weber-Bargioni, A.; Javey, A. Neutral Exciton Diffusion in Monolayer MoS_2. *ACS Nano* **2020,** *14*, 13433.

44. Pierret, R. F., *Semiconductor device fundamentals*. Pearson Education India: 1996.

45. Sveinbjörnsson, K.; Aitola, K.; Zhang, X.; Pazoki, M.; Hagfeldt, A.; Boschloo, G.; Johansson, E. M. J. Probing Photocurrent Generation, Charge Transport, and Recombination Mechanisms in Mesostructured Hybrid Perovskite through Photoconductivity Measurements. *The Journal of Physical Chemistry Letters* **2015,** *6*, 4259.

46. Chen, X.; Lian, Z.; Meng, Y.; Ma, L.; Shi, S.-F. Excitonic Complexes in Two-Dimensional Transition Metal Dichalcogenides. *Nature Communications* **2023,** *14*, 8233.

47. Park, H.; Zhu, J.; Wang, X.; Wang, Y.; Holtzmann, W.; Taniguchi, T.; Watanabe, K.; Yan, J.; Fu, L.; Cao, T.; Xiao, D.; Gamelin, D. R.; Yu, H.; Yao, W.; Xu, X. Dipole ladders with large Hubbard interaction in a moiré exciton lattice. *Nature Physics* **2023,** *19*, 1286.

48. Baloch, A. A. B.; Alharbi, F. H.; Grancini, G.; Hossain, M. I.; Nazeeruddin, M. K.; Tabet, N. Analysis of Photocarrier Dynamics at Interfaces in Perovskite Solar Cells by Time-Resolved Photoluminescence. *The Journal of Physical Chemistry C* **2018,** *122*, 26805.

49. Chen, J.; Lv, J.; Liu, X.; Lin, J.; Chen, X. A study on theoretical models for investigating time-resolved photoluminescence in halide perovskites. *Physical Chemistry Chemical Physics* **2023,** *25*, 7574.

50. Chen, W.; Wu, Y.; Yue, Y.; Liu, J.; Zhang, W.; Yang, X.; Chen, H.; Bi, E.; Ashraful, I.; Grätzel, M.; Han, L. Efficient and stable large-area perovskite solar cells with inorganic charge extraction layers. *Science* **2015,** *350*, 944.

51. Stranks, S. D.; Eperon, G. E.; Grancini, G.; Menelaou, C.; Alcocer, M. J. P.; Leijtens, T.; Herz, L. M.; Petrozza, A.; Snaith, H. J. Electron-Hole Diffusion Lengths Exceeding 1 Micrometer in an Organometal Trihalide Perovskite Absorber. *Science* **2013,** *342*, 341.

Figure Caption

Figure 1. Sample fabrication and characterization. (a) Schematic experimental setup. (b) Optical image of a $MAPbI_3$ coated 5-layer MoS_2 device (D1). (c) XRD θ-2θ scan of a 500 nm $MAPbI_3$ film on SiO_2. (d) AFM topography image of the boxed area in (b). The dashed lines mark the edges of MoS_2 and Au electrodes. (e) I_{dark} vs V_{SD} for device D1 before and after the deposition of $MAPbI_3$. (f) Schematic band diagram for $MAPbI_3/MoS_2$ heterointerface. The shadowed area highlights the depletion region. The arrow indicates the built-in electric field direction.

Figure 2. Photocurrent mapping. (a) I_{ph} mapping in log scale taken on device D1 (laser wavelength: 633 nm; beam size: 1 μm; scan step size: 0.8 μm). The dotted lines illustrate the edges of MoS_2 and Au electrodes. (b) I_{ph} profiles (open symbols) along the vertical dashed line (i) in (a) with fits (dashed lines). (c) I_{ph} profiles (open symbols) along the horizontal dashed lines in (a) with fits (dashed lines): (ii) single-layer $MAPbI_3$, (iii) $MAPbI_3/MoS_2$ heterostructure. Inset: Expanded view of I_{ph} profile (ii) in linear scale with the fit. The shadowed area marks the electrodes.

Figure 3. Photocurrent annihilation processes. (a) I_{ph} vs P under local illumination (laser wavelength: 633 nm; beam size 1 μm) on single-layer $MAPbI_3$ (blue triangles) and heterostructure region (red circles), and global illumination (laser wavelength: 633 nm; beam size 800 μm) (black squares). Dashed lines represent fits to $I_{ph} \propto P^{\beta}$, with β values labeled. (b) Schematic of photocharge generation and radiative recombination in single-layer $MAPbI_3$. (c) Schematic of interlayer photocharge transfer and quadruple-molecular recombination in $MAPbI_3/MoS_2$heterostructure.

Figure 4. Time-resolved photocurrent response. (a) Normalized I_{ph} switching of device D1 upon turning on (shadowed area) and off the global illumination light (laser wavelength: 405 nm; beam size: 800 μm). Pulse duration: 2 seconds. (b) One I_{ph} switching period (open circles) with exponential fits (dashed lines). (c) Transient photocurrent of device D2 under localized stimulation (laser wavelength: 408 nm; beam size: 1 μm) in single-layer $MAPbI_3$ (black and blue lines) and heterostructure (red line) regions. The laser spot locations are indicated in the optical device image (inset).

Figure 5. Time-resolved photoluminescence. (a) Normalized PL intensity vs time after excitation taken on device D3 (pulsed laser wavelength: 408 nm; beam size: 1 μm). Inset: Optical device image, with the spots for the TRPL measurements marked. (b) τ_{PL} as a function of location along the white arrow in the inset of (a). The dashed lines mark the MoS_2 edges.

Figure 1

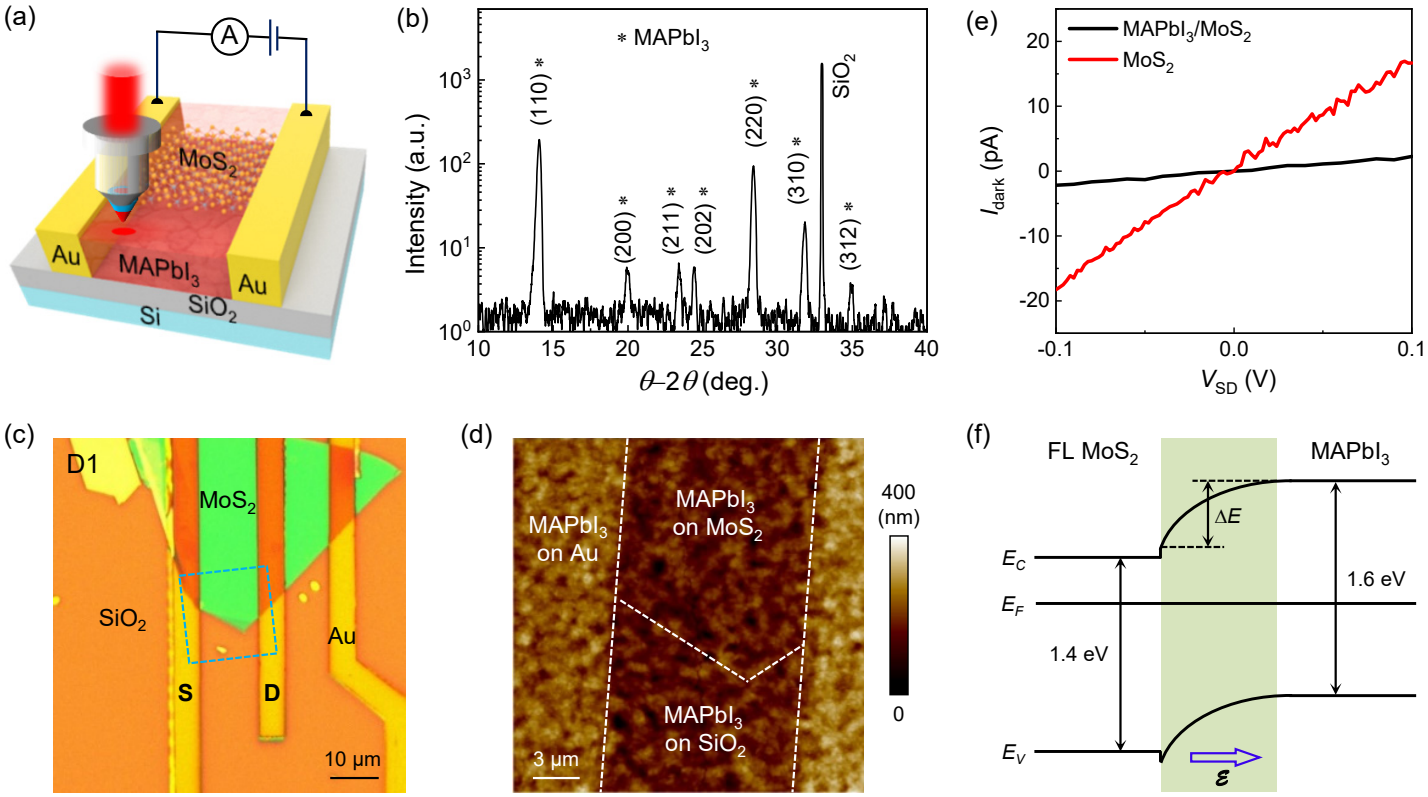
(a)
A
MoS2
Au
MAPbI3
Au
Si
SiO2
(b)
* MAPbI3
Intensity (a.u.)
(110) *
(200) *
(211) *
(202) *
(220) *
(310) *
SiO2
(312) *
θ–2θ (deg.)
(e)
MAPbI3/MoS2
MoS2
Idark (pA)
VSD (V)
(c)
D1
MoS2
SiO2
Au
S
D
10 μm
(d)
MAPbI3 on Au
MAPbI3 on MoS2
MAPbI3 on SiO2
3 μm
400 (nm)
0
(f)
FL MoS2
MAPbI3
ΔE
EC
EF
EV
1.4 eV
1.6 eV
ε

Figure 2

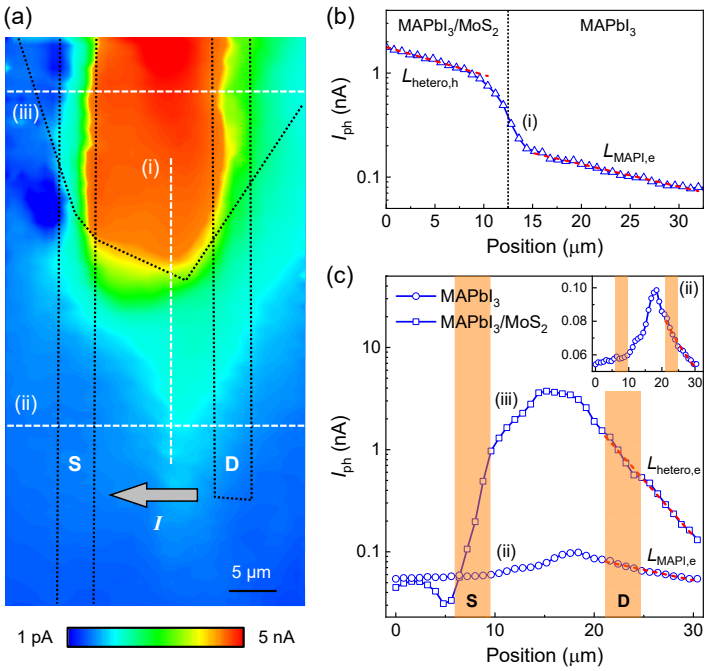
(a)
(iii)
(i)
(ii)
S
D
I
5 μm
1 pA
5 nA
(b)
MAPbI3/MoS2
MAPbI3
Lhetero,h
(i)
LMAPI,e
Iph (nA)
Position (μm)
(c)
MAPbI3
MAPbI3/MoS2
(ii)
(iii)
Lhetero,e
LMAPI,e
S
D
Iph (nA)
Position (μm)

Figure 3

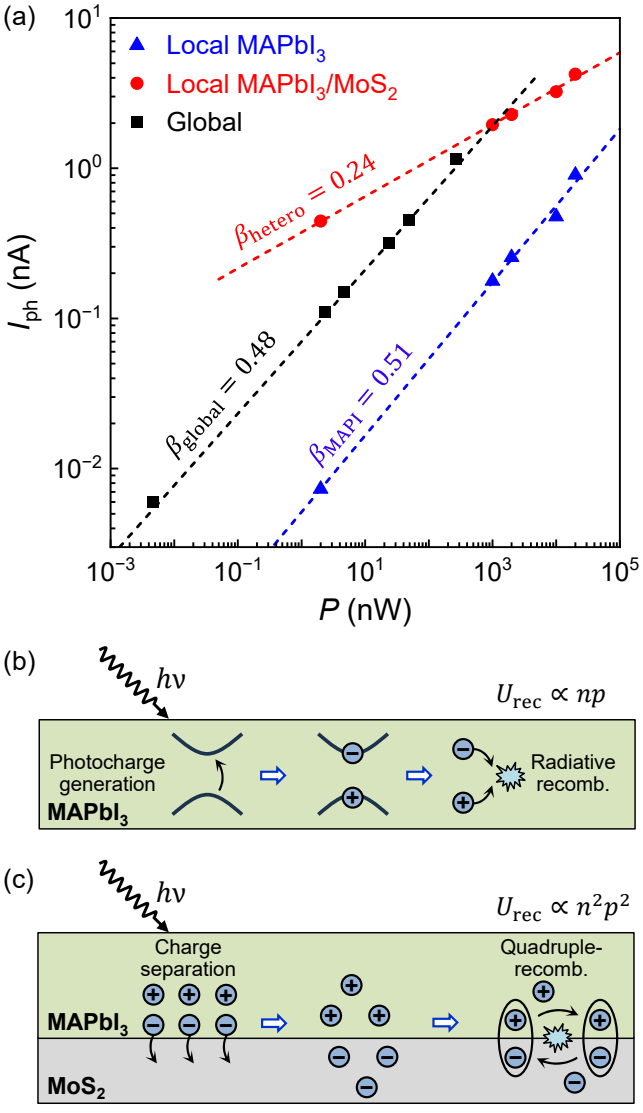
(a)
Local MAPbI3
Local MAPbI3/MoS2
Global
βhetero = 0.24
βglobal = 0.48
βMAPI = 0.51
Iph (nA)
P (nW)
(b)
hν
Urec ∝ np
Photocharge generation
MAPbI3
Radiative recomb.
(c)
hν
Urec ∝ n2p2
Charge separation
MAPbI3
MoS2
Quadruple-recomb.

Figure 4

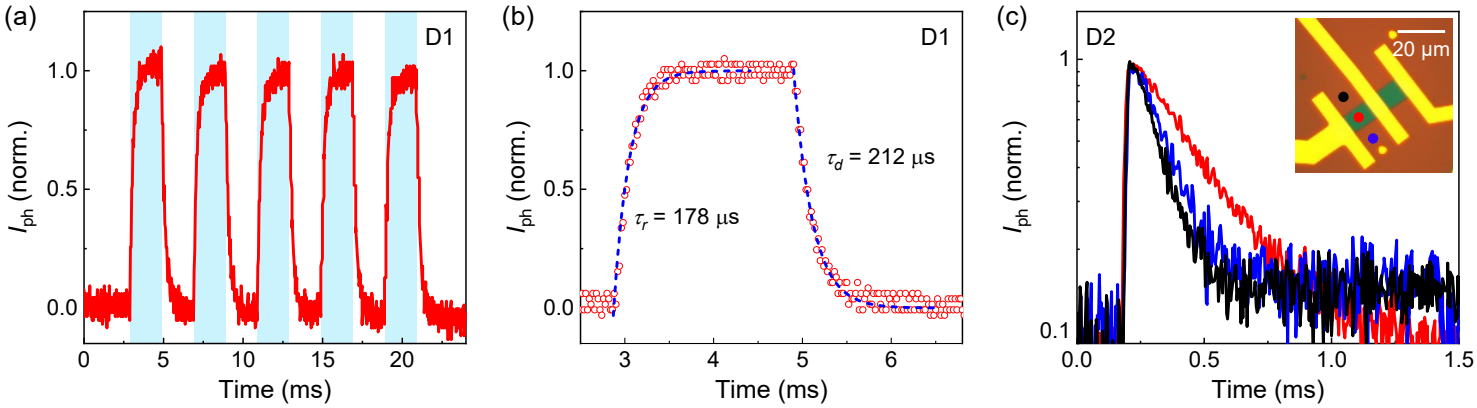
(a)
D1
1.0
0.5
0.0
I_{ph} (norm.)
0
5
10
15
20
Time (ms)
(b)
D1
1.0
0.5
0.0
I_{ph} (norm.)
τ_r = 178 μs
τ_d = 212 μs
3
4
5
6
Time (ms)
(c)
D2
20 μm
1
0.1
I_{ph} (norm.)
0.0
0.5
1.0
1.5
Time (ms)

Figure 5

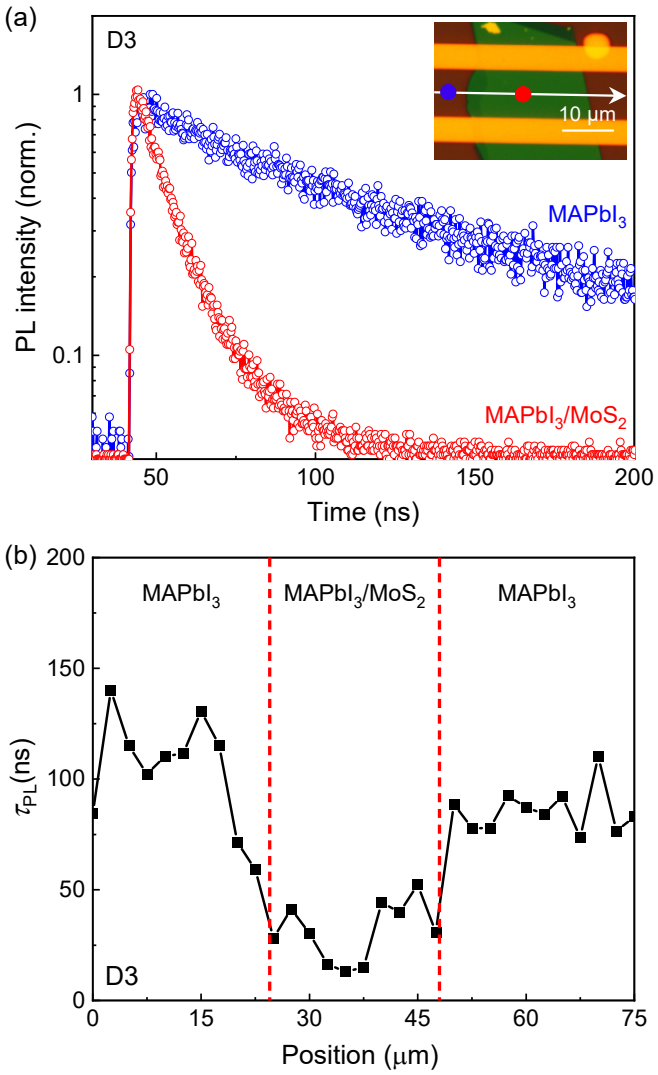
(a)
D3
10 μm
MAPbI3
MAPbI3/MoS2
PL intensity (norm.)
1
0.1
50
100
150
200
Time (ns)
(b)
MAPbI3
MAPbI3/MoS2
MAPbI3
τPL (ns)
200
150
100
50
0
D3
0
15
30
45
60
75
Position (μm)